

# ALMA CO Observations of a Giant Molecular Cloud in M33: Evidence for High-Mass Star Formation Triggered by Cloud-Cloud Collisions

Hidetoshi SANO<sup>1</sup>, Kisetsu TSUGE<sup>2</sup>, Kazuki TOKUDA<sup>3,4</sup>, Kazuyuki MURAOKA<sup>4</sup>, Kengo TACHIHARA<sup>2</sup>, Yumiko YAMANE<sup>2</sup>, Mikito KOHNO<sup>2,5</sup>, Shinji FUJITA<sup>2</sup>, Rei ENOKIYA<sup>2</sup>, Gavin ROWELL<sup>6</sup>, Nigel MAXTED<sup>7</sup>, Miroslav D. FILIPOVIĆ<sup>8</sup>, Jonathan KNIES<sup>9</sup>, Manami SASAKI<sup>9</sup>, Toshikazu ONISHI<sup>4</sup>, Paul P. PLUCINSKY<sup>10</sup> and Yasuo FUKUI<sup>2,3</sup>

<sup>1</sup>National Astronomical Observatory of Japan, Mitaka, Tokyo 181-8588, Japan

<sup>2</sup>Department of Physics, Nagoya University, Furo-cho, Chikusa-ku, Nagoya 464-8601, Japan

<sup>3</sup>Institute for Advanced Research, Nagoya University, Furo-cho, Chikusa-ku, Nagoya 464-8601, Japan

<sup>4</sup>Department of Physical Science, Graduate School of Science, Osaka Prefecture University, 1-1 Gakuen-cho, Naka-ku, Sakai, Osaka 599-8531, Japan

<sup>5</sup>Astronomy Section, Nagoya City Science Museum, 2-17-1 Sakae, Naka-ku, Nagoya, Aichi 460-0008, Japan

<sup>6</sup>School of Physical Sciences, The University of Adelaide, North Terrace, Adelaide, SA 5005, Australia

<sup>7</sup>School of Science, University of New South Wales, Australian Defence Force Academy, Canberra, ACT 2600, Australia

<sup>8</sup>Western Sydney University, Locked Bag 1797, Penrith South DC, NSW 2751, Australia

<sup>9</sup>Dr. Karl Remeis-Sternwarte, Erlangen Centre for Astroparticle Physics, Friedrich-Alexander-Universität Erlangen-Nürnberg, Sternwartstraße 7, D-96049 Bamberg, Germany

<sup>10</sup>Harvard-Smithsonian Center for Astrophysics, 60 Garden St., Cambridge, MA 02138, USA

\*E-mail: hidetoshi.sano@nao.ac.jp

RECEIVED 2019 AUGUST 27 ; ACCEPTED 2020 APRIL 16

## Abstract

We report the first evidence for high-mass star formation triggered by collisions of molecular clouds in M33. Using the Atacama Large Millimeter/submillimeter Array, we spatially resolved filamentary structures of giant molecular cloud 37 in M33 using  $^{12}\text{CO}(J = 2-1)$ ,  $^{13}\text{CO}(J = 2-1)$ , and  $\text{C}^{18}\text{O}(J = 2-1)$  line emission at a spatial resolution of  $\sim 2$  pc. There are two individual molecular clouds with a systematic velocity difference of  $\sim 6 \text{ km s}^{-1}$ . Three continuum sources representing up to  $\sim 10$  high-mass stars with the spectral types of B0V–O7.5V are embedded within the densest parts of molecular clouds bright in the  $\text{C}^{18}\text{O}(J = 2-1)$  line emission. The two molecular clouds show a complementary spatial distribution with a spatial displacement of  $\sim 6.2$  pc, and show a V-shaped structure in the position-velocity diagram. These observational features traced by CO and its isotopes are consistent with those in high-mass star-forming regions created by cloud-cloud collisions in the Galactic and Magellanic Cloud H<sub>II</sub> regions. Our new finding in M33 indicates that the cloud-cloud collision is a promising process to trigger

high-mass star formation in the Local Group.

**Key words:** ISM: H<sub>II</sub> regions—Stars: formation—ISM: individual objects (M33, M33GMC 37)

## 1 Introduction

It is a long-standing question how high-mass stars are formed in galaxies. Three different hypothesis are thought to be mechanisms of the high-mass star formation: the monolithic collapse, competitive accretion, and the stellar mergers (e.g., Zinnecker, & Yorke 2007 and references therein). However, these theoretical models have remained controversial due to lacking conclusive observational evidence.

Recently, an alternative idea of high-mass star formation triggered by “cloud-cloud collisions” has received much attention since the discovery of 50 or more pieces of observational evidence (e.g., Fukui et al. 2018a; Enokiya et al. 2019 and references therein). The colliding clouds have a supersonic velocity difference with an intermediate velocity component—bridging feature—created by the collisional deceleration. The complementary spatial distribution of two clouds (or spatial anti-correlation between the two clouds) is one of the important signatures of collisions because one of the colliding clouds can create a hollowed-out structure in the other cloud. Furthermore, a V-shaped structure can be seen in the position-velocity diagram due to the deceleration and hollowed-out structure. Theoretical studies also support these observational signatures, and predict that cloud-cloud collision increases the effective Jeans mass so high-mass stars can form the high-mass stars in the shock-compressed layer (e.g., Habe & Ohta 1992; Anathpindika 2010; Inoue & Fukui 2013; Takahira et al. 2014; Shima et al. 2018; Inoue et al. 2018).

Investigating the universality of the cloud-cloud collision scenario, we need further observational examples under various environments and their scales. In the individual Galactic star-forming regions such as Orion and Vela, the high-mass star formation can be understood by at least five cloud-cloud collisions on  $\sim$ 1–100 pc scales (Fukui et al. 2016, 2018a; Fujita et al. 2017; Sano et al. 2018; Hayashi et al. 2018; Enokiya et al. 2018). It is remarkable that collisions of molecular clouds are seen not only in our Milky Way, but also in the Magellanic Clouds (e.g., Fukui et al. 2015; Saigo et al. 2017). Furthermore, the tidally driven galactic-scale (a few kpc scales) collisions of H<sub>I</sub> clouds are found in the Magellanic and M31–M33 systems (Fukui et al. 2017, 2019; Tsuge et al. 2019; Tachihara et al. 2018; Tokuda et al. 2019). We can therefore reveal sites of cloud-cloud collisions even in external galaxies if the spatial resolution of CO/H<sub>I</sub> data is high enough (e.g.,

a few pc scales).

Here, we report the first evidence for the high-mass star formation triggered by collisions of molecular clouds in M33. Sections 2 and 3 describe observations and data reduction of the ALMA CO and continuum datasets and their results. Section 4.1 gives properties of high-mass stars in the region; Section 4.3 presents a possible scenario of cloud-cloud collision as the formation mechanism of high-mass stars. A summary and conclusions are provided in Section 5.

## 2 Observations and Data Reduction

We carried out ALMA Band 6 (211–275 GHz) observations toward M33GMC 37 in Cycle 6 as part of the CO survey toward the SNRs in M33 (PI: H. Sano, #2018.1.00378.S). We used the single-pointing observation mode with 45–49 antennas of the 12-m arrays. The center position of the pointing is  $(\alpha_{J2000}, \delta_{J2000}) \sim (01^{\mathrm{h}}33^{\mathrm{m}}35^{\mathrm{s}}.9, 30^{\circ}36'27''5)$ . The baseline length ranges from 15.06 to 1397.85 m, corresponding to  $u$ – $v$  distances from 11.6 to 1074.9  $k\lambda$ . The maximum recoverable scale (a.k.a. largest angular scale) is calculated to be  $3''.73$ . Two quasars, J2253+1608 and J0237+2848 were observed as bandpass and flux calibrators. We also observed the quasar J0112+3208 as a phase calibrator. There were two spectral windows including the  $^{12}\mathrm{CO}(J = 2-1)$ ,  $^{13}\mathrm{CO}(J = 2-1)$ , and  $\mathrm{C}^{18}\mathrm{O}(J = 2-1)$  line emission with a bandwidth of 117.19 MHz. The frequency resolution was 70.6 kHz for  $^{12}\mathrm{CO}(J = 2-1)$  and 141.1 kHz for  $^{13}\mathrm{CO}(J = 2-1)$  and  $\mathrm{C}^{18}\mathrm{O}(J = 2-1)$ . We also observed two spectral windows as continuum bands, of which frequency ranges are 231.0–233.0 GHz and 216.3–218.2 GHz. Although these continuum bands contain line emission of H(30 $\alpha$ ) and SiO( $J = 5-4$ ), we could not detect the two lines significantly.

The data reduction was performed using the Common Astronomy Software Application (CASA; McMullin et al. 2007) package version 5.5.0. We used the “multiscale CLEAN” algorithm implemented in the CASA package (Cornwell 2008). The synthesized beam of final dataset is  $0''.59 \times 0''.42$  with a position angle (P.A.) of  $0.4^{\circ}$  for  $^{12}\mathrm{CO}(J = 2-1)$ ,  $0''.62 \times 0''.44$  with a P.A. of  $0.1^{\circ}$  for  $^{13}\mathrm{CO}(J = 2-1)$ ,  $0''.63 \times 0''.44$  with a P.A. of  $1.1^{\circ}$  for  $\mathrm{C}^{18}\mathrm{O}(J = 2-1)$ , and  $0''.59 \times 0''.43$  with a P.A. of  $-1.4^{\circ}$  for the 1.3 mm continuum. The typical spatial resolution is  $\sim 2$  pc at the distance of M33 ( $817 \pm 59$  kpc, Freedman et al. 2001). The

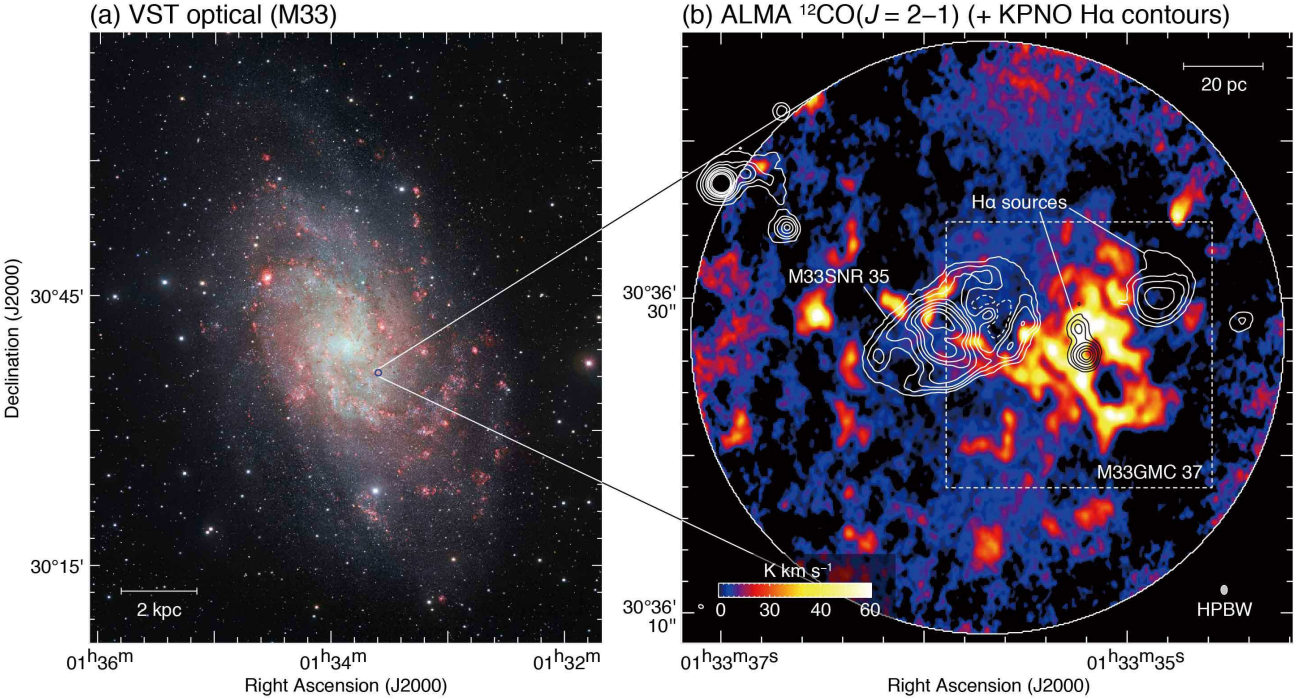


**Fig. 1.** False color image of M33 obtained with the VLT Survey Telescope (VST, credit: ESO). The red, orange, and cyan represent  $\text{H}\alpha$ , r-band, and g-band, respectively. The blue circle indicates the ALMA FoV. The scale bar is shown in the bottom left corner. (b) Integrated intensity map of  $^{12}\text{CO}(J=2-1)$  obtained with ALMA. The integration velocity range is  $-145$ — $126 \text{ km s}^{-1}$ . The superposed white and black contours indicate the  $\text{H}\alpha$  intensity obtained by the Kitt Peak National Observatory (KPNO, Massey et al. 2006). The contour levels are 300, 400, 500, 700, 900, 1100, 1500, and 1900  $\text{ergs s}^{-2} \text{ cm}^{-2}$ . The dashed box containing M33GMC 37 represents the region to be shown in Figures 2, 4, and 8. We also annotated positions of M33SNR 35 and  $\text{H}\alpha$  sources. The scale bar and beam size are also shown in the top right and bottom right corners, respectively.

typical noise fluctuations of the line emission and continuum are  $\sim 0.15 \text{ K}$  at the velocity resolution of  $1 \text{ km s}^{-1}$  and  $0.017 \text{ mJy beam}^{-1}$ , respectively. To estimate the missing flux density, we used the  $^{12}\text{CO}(J=2-1)$  dataset obtained with the IRAM 30-m radio telescope (Gratier et al. 2010; Druard et al. 2014). Following the methods of Druard et al. (2014), we applied a forward efficiency of 0.92 and a main beam efficiency of 0.56 to convert the main beam temperature scale. We compared the integrated intensities of IRAM and ALMA CO data that are smoothed to match the FWHM resolution of  $12''$ . As a result, We found no significant difference within the error margin, and hence the missing flux density is considered to be negligible.

### 3 Results

Figure 1a shows an optical composite image of M33 obtained with the VLT Survey Telescope (VST). The ALMA FoV includes several  $\text{H}\alpha$  regions located in a spiral arm near the galactic center. Figure 1b shows a large-scale map of ALMA  $^{12}\text{CO}(J=2-1)$  superposed on  $\text{H}\alpha$  contours. A giant molecular cloud (GMC)—M33GMC 37—is mainly located on the western-half of the ALMA FoV with filamentary structures. Some of CO filaments are likely associated with M33SNR 35, which will be described in a forthcoming paper (H. Sano et al. in preparation). We also note that a bright  $\text{H}\alpha$  source with two local peaks at the positions of  $(\alpha_{\text{J}2000}, \delta_{\text{J}2000}) \sim (01^{\text{h}}33^{\text{m}}35^{\text{s}}.24, 30^{\circ}36'28''.0)$  and  $(01^{\text{h}}33^{\text{m}}35^{\text{s}}.20, 30^{\circ}36'26''.3)$  are superposed on the GMC.

To derive the mass of GMC, we used the following equations:

$$M = m_{\text{H}} \mu D^2 \Omega \sum_i [N_i(\text{H}_2)], \quad (1)$$

$$N(\text{H}_2) = X_{\text{CO}} \cdot W(\text{CO}_{10}), \quad (2)$$

where  $m_{\text{H}}$  is the mass of hydrogen,  $\mu$  is the mean molecular weight of  $\sim 2.74$ ,  $D$  is the distance to M33 in units of cm,  $\Omega$  is the solid angle of each data pixel,  $N_i(\text{H}_2)$  is the column density of molecular hydrogen for each data pixel  $i$  in units of  $\text{cm}^{-2}$ ,  $X$  is the CO-to- $\text{H}_2$  conversion factor in units of  $(\text{K km s}^{-1})^{-1} \text{ cm}^{-2}$ , and  $W(\text{CO}_{10})$  is integrated intensity of  $^{12}\text{CO}(J=1-0)$  line emission. In the present study, we adopt  $D = 2.5 \times 10^{24} \text{ cm}$ , corresponding to the distance of 817 kpc (Freedman et al. 2001). Following the previous study by Gratier et al. (2012), we used  $X = 4.0 \times 10^{20} (\text{K km s}^{-1})^{-1} \text{ cm}^{-2}$ . We also derived a typical intensity ratio of  $^{12}\text{CO}(J=2-1) / ^{12}\text{CO}(J=1-0) \sim 0.7$  toward

M33GMC 37 through the comparison with an archival  $^{12}\text{CO}(J = 1-0)$  cube data obtained with the Nobeyama Radio Observatory 45-m telescope (Tosaki et al. 2011). Finally, the derived size and mass of the GMCs are  $\sim 60$  pc and  $\sim 5 \times 10^5 M_\odot$ , respectively. These values are roughly consistent with the previous study by Miura et al. (2012) using the Atacama Submillimeter Telescope Experiment: size of  $63 \times 54$  pc and virial mass of  $(6.7 \pm 4.8) \times 10^5 M_\odot$ .

Figures 2a, 2d, and 2g show the maps of moment 0 (integrated intensity) for each line emission toward M33GMC 37. The area shown in Figure 2 is indicated by the dashed box in Figure 1. The  $^{12}\text{CO}(J = 2-1)$  clouds are detected as diffuse emission with a ring-like structure in southwest, while the  $^{13}\text{CO}(J = 2-1)$  clouds are only bright in the ring-like structure. The  $\text{C}^{18}\text{O}(J = 2-1)$  clouds are concentrated in the central region of GMC where the  $^{12}\text{CO}(J = 2-1)$  and  $^{13}\text{CO}(J = 2-1)$  clouds are bright. We also find that there are three sources in 1.3 mm continuum as shown in Figure 2g'—GMC37-MMSs 1–3 (hereafter refer to as MMSs 1–3)—, which are detected at a  $5\sigma$  level or higher. The basic physical properties of three continuum sources are listed in Table 1. The peak brightness temperatures of the three sources are comparable, but the spatial extent of MMS 2 is twice as large than that of MMSs 1 and 3. It is possible that these millimeter continuum sources are physically related to the  $\text{H}\alpha$  emission. In particular, two of them (MMSs 2 and 3) are located in the vicinity of the two  $\text{H}\alpha$  peaks (as shown by diamonds in Figure 2g') associated with the brightest CO cloud, indicating that the exciting stars of MMSs 2–3 and  $\text{H}\alpha$  peaks are the same. These regions are also bright in the *Spitzer* 24  $\mu\text{m}$  image (Verley et al. 2007).

Figures 2b, 2e, and 2h show the maps of moment 1 (peak velocity). The peak velocities of  $^{12}\text{CO}(J = 2-1)$  and  $^{13}\text{CO}(J = 2-1)$  clouds are discontinuous with a velocity jump of  $\sim 10 \text{ km s}^{-1}$  toward the millimeter continuum sources and the eastern side of them, while that of  $\text{C}^{18}\text{O}(J = 2-1)$  line emission shows no significant velocity jump within the clouds. Figures 2c, 2f, and 2i show the maps of moment 2 (velocity dispersion). A larger velocity dispersion above  $3 \text{ km s}^{-1}$  is seen in several regions of both the  $^{12}\text{CO}(J = 2-1)$  and  $^{13}\text{CO}(J = 2-1)$  clouds, where the velocity jumps are identified (see also Figure 2b). On the other hand, there is no sign of such larger velocity dispersion in the  $\text{C}^{18}\text{O}(J = 2-1)$  clouds.

Figure 3 shows the typical CO spectra toward three positions A, B, and C. The position A represents the direction of MMS 1. The positions B and C correspond the regions with the largest velocity dispersion in  $^{13}\text{CO}(J = 2-1)$  line emission (see also Figure 2f) and with the maximum intensity of  $\text{C}^{18}\text{O}(J = 2-1)$  line emission (see also Figure 2g),

**Table 1.** Physical properties of 1.3 mm continuum sources

Name	$\alpha_{\text{J}2000}$ ( $^{\text{h}} \text{m} \text{s}$ )	$\delta_{\text{J}2000}$ ( $^{\circ} \text{'} \text{''}$ )	$F_{\text{peak}}$ ( $\text{mJy beam}^{-1}$ )	Size (pc)
(1)	(2)	(3)	(4)	(5)
GMC37-MMS 1	01 33 35.22	30 36 29.0	0.12	1.7
GMC37-MMS 2	01 33 35.22	30 36 27.8	0.13	3.0
GMC37-MMS 3	01 33 35.22	30 36 26.4	0.11	1.6

Note. — Col. (1): Name of millimeter continuum source. Cols. (2–3)

Positions of the maximum flux. Col. (4): Peak flux of 1.3 mm continuum. Col. (5): Size of continuum source defined as  $(S/\pi)^{0.5} \times 2$ , where  $S$  is the total surface area of continuum source surrounded by a contour of the  $5\sigma$  level.

respectively. The CO spectra of the position A is centered at  $\sim 132 \text{ km s}^{-1}$ , corresponding to the systemic velocity of the M33GMC 37 region which was derived by a rotation model of the  $\text{H}\text{I}$  disk (Gratier et al. 2010). We note that the  $^{12}\text{CO}(J = 2-1)$  line emission shows a wing-like profile with a velocity extent of more than  $5 \text{ km s}^{-1}$ . For the position B, we find double-peak profiles in both the  $^{12}\text{CO}(J = 2-1)$  and  $^{13}\text{CO}(J = 2-1)$  line emission, suggesting that there are two individual clouds toward the line-of-sight. We hereafter refer to the component at  $V_{\text{LSR}} = -143.0\text{--}134.0 \text{ km s}^{-1}$  as the “blue cloud” and that at  $V_{\text{LSR}} = -133.0\text{--}127.0 \text{ km s}^{-1}$  as the “red cloud.” On the other hand, the CO spectra of the position C—the brightest peak in  $\text{C}^{18}\text{O}(J = 2-1)$ —show a single peak profile for each line emission. Note that their central velocities of  $V_{\text{LSR}} \sim -133.5 \text{ km s}^{-1}$  are roughly corresponding to the mean velocity of red and blue clouds.

Figures 4a and 4b show spatial distributions of blue and red clouds. The blue cloud is elongated in the northwestern direction, while the red cloud is stretched in the southwestern direction. Both clouds have filamentary CO structures. The typical width and length of filaments are  $\sim 3$  pc and  $\sim 10$  pc, respectively. The total mass is estimated to be  $\sim 2.4 \times 10^5 M_\odot$  for the blue cloud and  $\sim 1.9 \times 10^5 M_\odot$  for the red cloud using equations (1) and (2). Note that MMS 2 is likely associated not only with the brightest peak of blue cloud, but also with that of red cloud. The other continuum sources—MMSs 1 and 3—appear to be overlapped with both the red and blue clouds. The peak column density of molecular hydrogen is  $\sim 4.5 \times 10^{22} \text{ cm}^{-2}$  for the blue-cloud, and  $\sim 4.1 \times 10^{22} \text{ cm}^{-2}$  for the red-cloud. We also find a small hole-like structure in the blue cloud centered at  $(\alpha_{\text{J}2000}, \delta_{\text{J}2000}) \sim (01^{\text{h}}35^{\text{m}}35^{\text{s}}28, 30^{\circ}36'27''1)$ . Note that the peak positions of  $\text{H}\alpha$  and millimeter continuum are placed on the edge of the hole-like structure, not on the center of it.

Figure 5 shows the position–velocity diagram of  $^{12}\text{CO}(J = 2-1)$ . The integration range in Right Ascension is from  $01^{\text{h}}33^{\text{m}}35^{\text{s}}243$  to  $01^{\text{h}}33^{\text{m}}35^{\text{s}}341$ , corresponding to the spa-

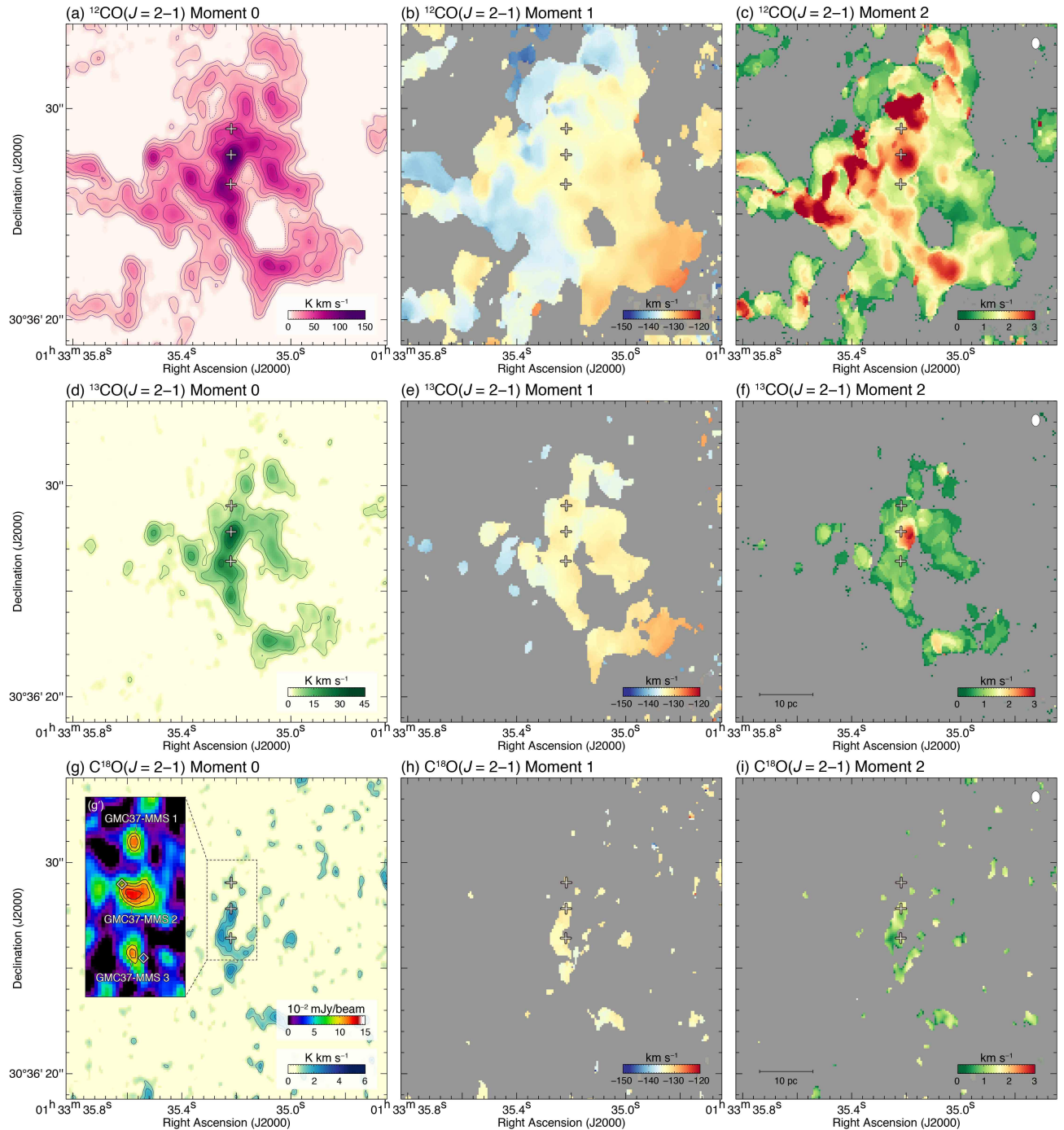


**Fig. 2.** Maps of moment 0 (integrated intensity: Figures 2a, 2d, and 2g), moment 1 (peak velocity: Figures 2b, 2e, and 2h), and moment 2 (velocity dispersion: Figures 2c, 2f, and 2i) toward M33GMC 35 for each line emission. The contour levels of moment 0 maps are 8, 14, 22, 32, 44, 58, 74, and 92 K km s<sup>-1</sup> for <sup>12</sup>CO( $J = 2-1$ ); 4, 8, 14, and 22 K km s<sup>-1</sup> for <sup>13</sup>CO( $J = 2-1$ ); and 1, 1.5, 2, 3, and 5 K km s<sup>-1</sup> for C<sup>18</sup>O( $J = 2-1$ ). Intensity distribution of 1.3 mm continuum is also shown in Figure 2g'. The contour levels of millimeter continuum are 9.0, 10.5, and 12.0  $\times 10^{-2}$  mJy beam<sup>-1</sup>. The crosses and diamonds represent the intensity peak positions of millimeter continuum sources and H $\alpha$ . The beam size and scale bar are also shown in the top right corner and bottom left corner of Figures 2c, 2f, and 2i, respectively.

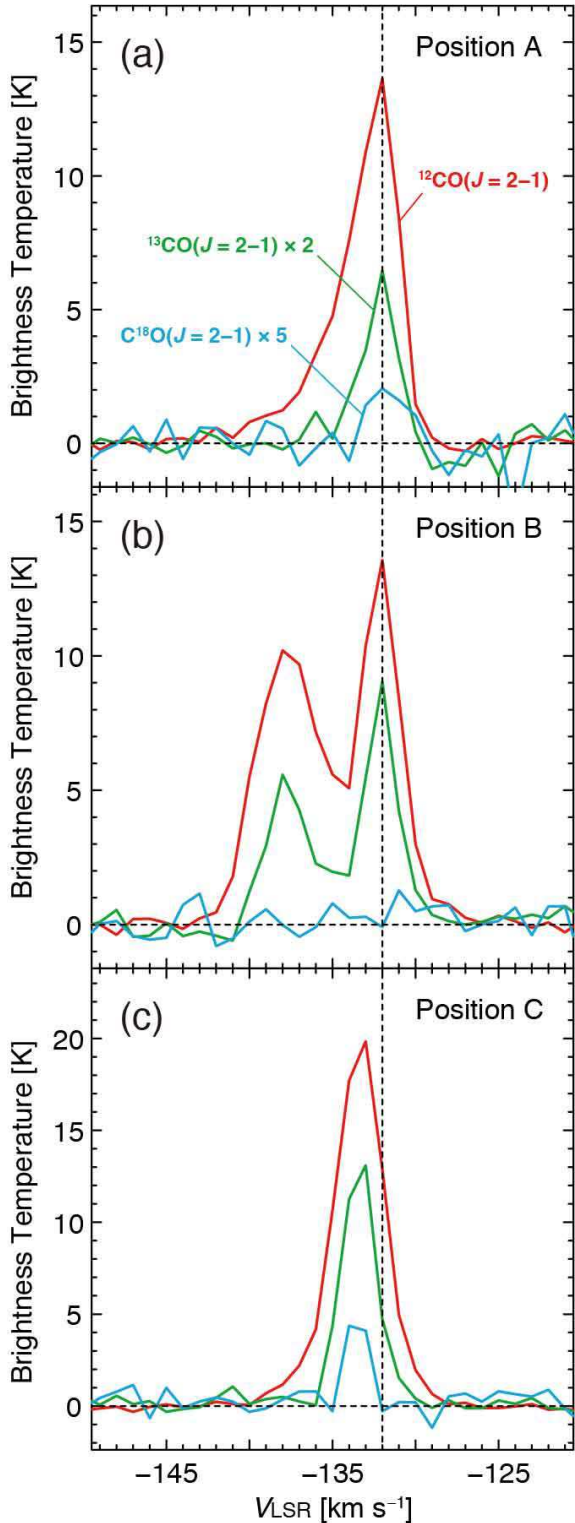


**Fig. 3.** Typical CO spectra in the positions of A  $[(\alpha_{J2000}, \delta_{J2000}) = (01^{\text{h}}33^{\text{m}}35^{\text{s}}22, 30^{\circ}36'29''.0)]$ , B  $[(\alpha_{J2000}, \delta_{J2000}) = (01^{\text{h}}33^{\text{m}}35^{\text{s}}19, 30^{\circ}36'27''.6)]$ , and C  $[(\alpha_{J2000}, \delta_{J2000}) = (01^{\text{h}}33^{\text{m}}35^{\text{s}}25, 30^{\circ}36'26''.6)]$ . The  $^{13}\text{CO}(J = 2-1)$  and  $\text{C}^{18}\text{O}(J = 2-1)$  brightness temperature are multiplied by a factor of two and five, respectively. The vertical dashed line indicates the systemic velocity of M33GMC 37.

tial extent of the small hole-like structure appeared in the blue cloud (see also Figure 4a). The blue cloud is clearly seen whose radial velocity is centered at  $V_{\text{LSR}} \sim -137 \text{ km s}^{-1}$ . We find a V-shaped structure in the position–velocity diagram (see dashed black lines in Figure 5). The center velocity of red cloud ( $V_{\text{LSR}} \sim -132 \text{ km s}^{-1}$ ) is corresponding to the vertex of the V-shaped structure. The cavity-like structure and intensity peak of  $^{12}\text{CO}(J = 2-1)$  are seen at  $(\delta_{J2000}, V_{\text{LSR}}) \sim (30^{\circ}36'27''.1, -135.0 \text{ km s}^{-1})$  and  $\sim (30^{\circ}36'26''.0, -134.0 \text{ km s}^{-1})$ , respectively.

## 4 Discussion

### 4.1 Presence of high-mass stars and their spectral types

Although there is no previous study of the stars embedded within the H $\alpha$  region in M33, detection of bright H $\alpha$  emission, 1.3 mm continuum sources MMSs 1–3, and 24  $\mu\text{m}$  emission indicates several high-mass stars are associated with the two molecular clouds. To confirm the presence of high-mass stars, we compared them with archival optical datasets obtained with the *Hubble Space Telescope* (*HST*). Figure 6 shows the high-spatial resolution optical images obtained with the *HST* WFPC2 and WFC3 detectors. The coordinate offsets of all datasets obtained with *HST* were corrected by comparing the position of the bright point sources with those catalogued in *Gaia* Data Release 2 (Gaia Collaboration et al. 2018). We can clearly see  $\sim 10$  high-mass stars bright in the U-band, H $\alpha$ , and IR-band within the Kitt Peak National Observatory (KPNO) H $\alpha$  contours. Hereafter, we assume that ten high-mass stars are associated with the H $\alpha$ , 1.3 mm continuum sources, and 24  $\mu\text{m}$  emission.

According to Verley et al. (2007), the luminosity of the 24  $\mu\text{m}$  emission is  $\sim 1.7 \times 10^{38} \text{ erg s}^{-1}$  and that of the H $\alpha$  emission is  $\sim 4.6 \times 10^{37} \text{ erg s}^{-1}$  using the *Spitzer* MIPS and KPNO H $\alpha$  datasets. To estimate the spectral types of high-mass stars, we used two different methods. One estimates the total infrared luminosity  $L(\text{TIR})$  using the measured 24  $\mu\text{m}$  luminosity  $L(24 \mu\text{m})$  and the following equation (Verley et al. 2007):

$$\log L(\text{TIR}) = \log L(24 \mu\text{m}) + 0.908 \quad (3)$$

The total infrared luminosity of the high-mass stars is estimated to be  $\sim 1.4 \times 10^{39} \text{ erg s}^{-1}$ , which corresponds to ten O7.5V stars (Martins et al. 2005), assuming that the ten high-mass stars have the same spectral types.

The other method is utilized Lyman continuum luminosities  $N_{\text{Lyman}}$  (in units of photons) that are derived from extinction corrected H $\alpha$  luminosities  $L_{\text{H}\alpha}$  (in units of  $\text{erg s}^{-1}$ ) using the following equation (Mayya & Prabhu 1996):

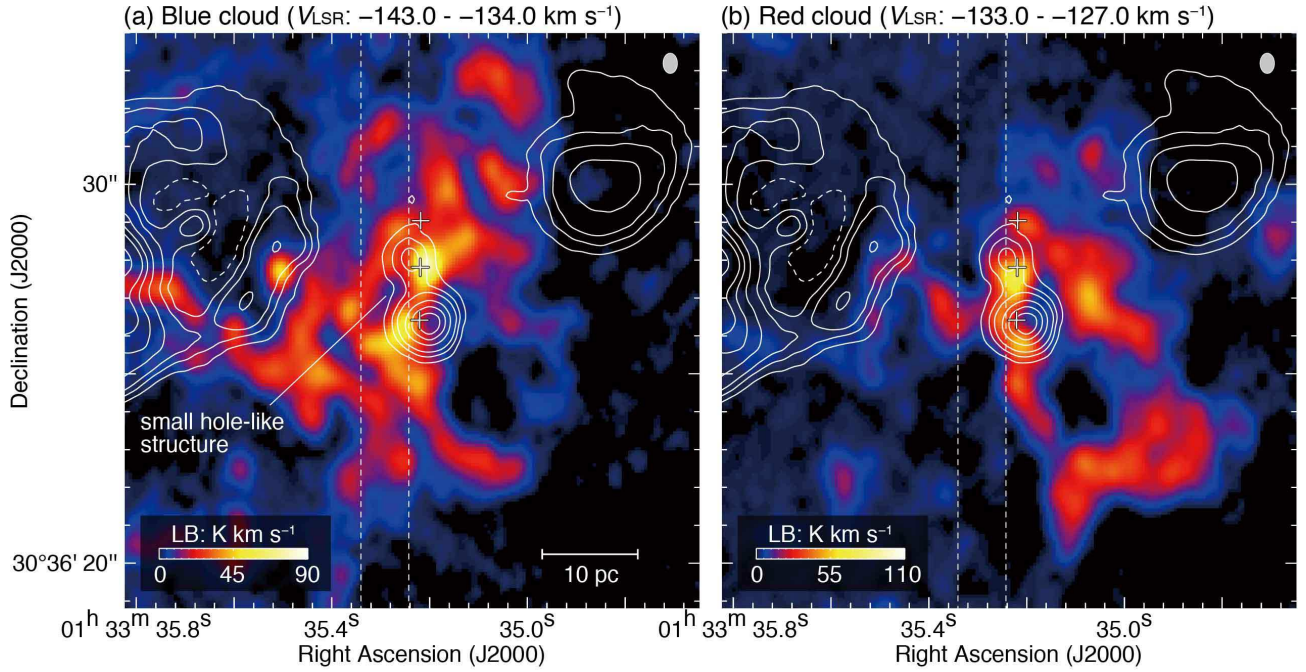


**Fig. 4.** Integrated intensity maps of  $^{12}\text{CO}(J = 2-1)$ . The velocity range is  $-143$ – $-134 \text{ km s}^{-1}$  for (a) and  $-133$ – $-127 \text{ km s}^{-1}$  for (b). The vertical dashed lines indicate the integration range in R.A. for Figure 5. The crosses represent the positions of 1.3 mm continuum. The white contours indicate  $\text{H}\alpha$  emission as shown in Figure 1b. The scale bar and beam size are also shown in the bottom and top right corners for each panel.

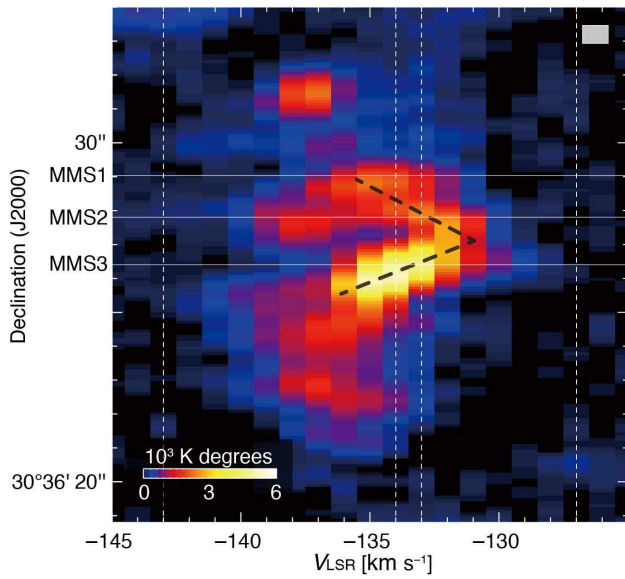


**Fig. 5.** Declination–velocity diagram of  $^{12}\text{CO}(J = 2-1)$ . The integration range is  $01^{\text{h}}33^{\text{m}}35^{\text{s}}.243$  to  $01^{\text{h}}33^{\text{m}}35^{\text{s}}.341$ . The vertical lines indicate integration velocity ranges for Figure 4. The three horizontal solid lines indicate the Declination positions of MMSs 1–3. The beam size is shown in the top right corner.

$$N_{\text{Lyman}} = 7.3 \times 10^{11} L_{\text{H}\alpha} \quad (4)$$

We then obtain  $N_{\text{Lyman}} = 1.1 \times 10^{49}$  photons, corresponding to ten B0V stars (Martins et al. 2005). To summaries, the spectral types of high-mass stars embedded within M33GMC 37 are estimated to be B0V–O7.5V assuming that there are ten high-mass stars with the same spectral types. Further detailed photometric and spectroscopic observations are needed to clarify the number of high-mass stars and their spectral types.

#### 4.2 Can stellar feedback explain the large velocity separation of the two clouds?

In the present study, we spatially resolved filamentary CO structures of M33GMC 37 using ALMA with spatial resolution of  $\sim 2 \text{ pc}$  ( $\Delta\theta \sim 0.5''$ ). There are two individual molecular clouds—red and blue clouds—with a velocity separation of  $\sim 6 \text{ km s}^{-1}$  and the mass of  $\sim 2 \times 10^5 M_{\odot}$  for each. The densest part of the GMC is significantly detected in  $\text{C}^{18}\text{O}(J = 2-1)$ , containing up to  $\sim 10$  high-mass stars with the spectral types of B0V–O7.5V. In this section, we shall discuss whether the velocity separation of two clouds can be explained by acceleration due to the stellar feedback.

First, we claim that the total momentum of stellar winds is significantly lower than that of the two molecular clouds. The typical wind momentum of an O-type star

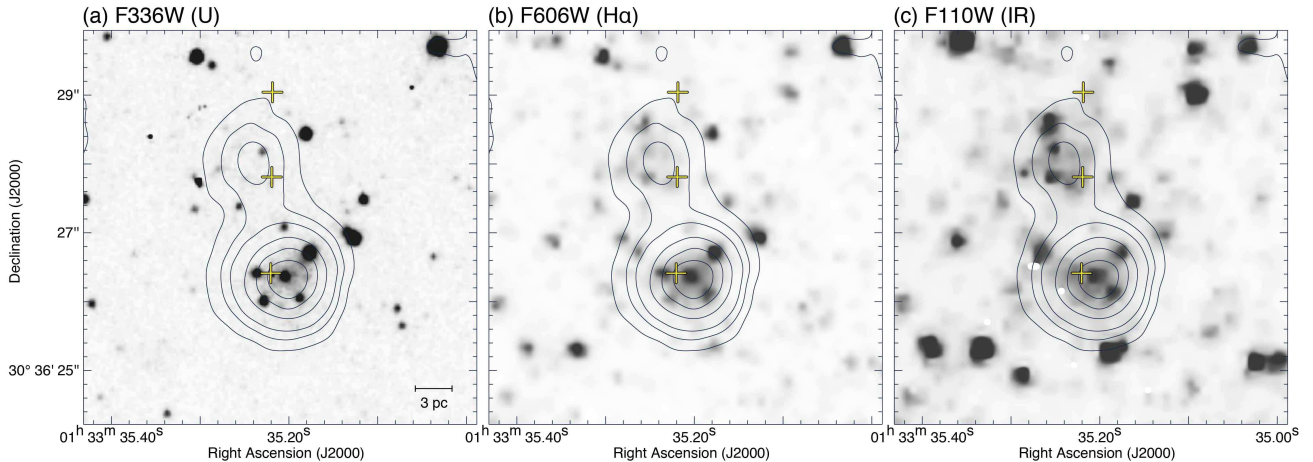


**Fig. 6.** Maps of optical images obtained with the *Hubble Space Telescope* (HST): (a) *HST*/WFC3 map with F336W filter (U-band), (b) *HST*/WFPC2 map with F606W filter (H $\alpha$ ), and (c) *HST*/WFC3 map with F110W filter (IR-band). The superposed contours and crosses are the same as in Figure 4. The scale bar is also shown in the bottom right corner in (a).

is calculated to be  $\sim 2 \times 10^3 M_{\odot} \text{ km s}^{-1}$ , by considering a mass accretion rate of  $\sim 10^{-6} M_{\odot} \text{ yr}^{-1}$ , a wind duration time of  $\sim 10^6 \text{ yr}$ , and a wind velocity of  $\sim 2,000 \text{ km s}^{-1}$  (see Kudritzki & Puls 2000 and references therein). In the case of M33GMC 37, the total wind momentum is therefore to be  $\sim 2 \times 10^4 M_{\odot} \text{ km s}^{-1}$  assuming that there are ten O-type stars (see Section 4.1). On the other hand, we derive a total cloud momentum of  $\sim 1.3 \times 10^6 M_{\odot} \text{ km s}^{-1}$ . Here we assume that the two clouds show an expanding motion with the expanding velocity of  $\sim 3 \text{ km s}^{-1}$ , corresponding to a half value of the velocity separation of the two clouds. Since the total cloud momentum is roughly two orders magnitude higher than the total wind momentum, we conclude that the velocity separation of two clouds cannot be explained by the expanding gas motion due to the stellar feedback.

This interpretation is also consistent with the velocity distributions of the two clouds. If the expansion of clouds is centered at an exciting star, a ring-like gas distribution will be expected not only in the spatial distribution such as the moment 0 map, but also in the position–velocity diagram (c.f., Figure 8 in Torii et al. 2015). For M33GMC 37, however, we could not find such distributions around the three millimeter continuum sources (see Figures 3a and 5). We also have created velocity channel maps in order to justify the velocity and spatial distributions of clouds, because expanding clouds will be spatially shifted from inward to outward in the velocity channel maps (e.g., Fukui et al. 2012; Sano et al. 2017a). Figure 7 shows the velocity channel maps for each CO line emission. We confirmed that there are no clear signs of such spatial shifts with increasing velocity. On the other hand, we note that a tiny CO clump near MMS 2 appears in all velocity ranges

of  $^{12}\text{CO}(J = 2-1)$  line emission, suggesting a possible evidence for the outflowing gas as well as the wing-like profile of MMS 1 (Figure 2a). Although the candidate of outflowing gas is very concentrated within 1 pc scales, the outflowing gas could not strongly affect to the dynamical motion of the two clouds. To summarize, the stellar feedback effect is negligible for the cloud kinematics, and therefore the velocity separation of two clouds cannot be explained by acceleration by stellar winds and outflowing gas.

#### 4.3 An Alternative Idea: High-mass Star Formation Triggered by Cloud-Cloud Collisions in M33GMC 37

In the previous section, we conclude that the velocity separation of two clouds have not caused by the stellar feedback effect. It is therefore reasonable to interpret that the individual two clouds have collided with each other and have formed the high-mass stars embedded within M33GMC 37. In this section, we discuss this second scenario.

To form high-mass stars via cloud-cloud collisions, a supersonic velocity separation of two colliding clouds is essential. According to magnetohydrodynamical numerical simulations, the effective Jeans mass in the shock-compressed layer is proportional to the third power of the effective sound speed (Inoue & Fukui 2013). Here, the effective sound speed is defined as  $\langle c_s^2 + c_A^2 + \Delta v^2 \rangle^{0.5}$ , where  $c_s$  is the sound speed,  $c_A$  is the Alfvén speed, and  $\Delta v$  is the velocity dispersion. A supersonic velocity separation of at least a few  $\text{km s}^{-1}$  therefore produces a large mass accretion rate on the order of  $\sim 10^{-4}\text{--}10^{-3} M_{\odot} \text{ yr}^{-1}$ ,

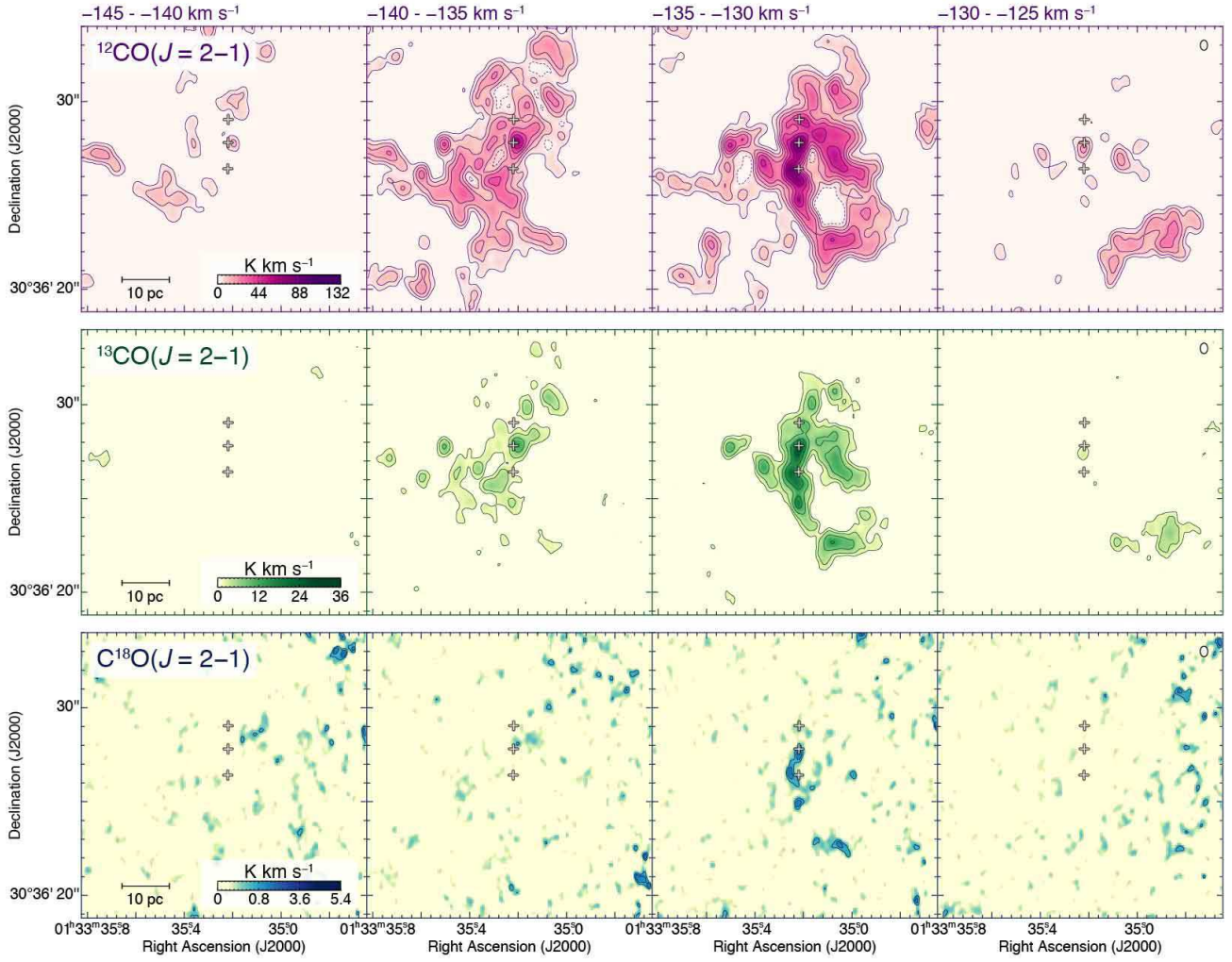


**Fig. 7.** Velocity channel maps of (a)  $^{12}\text{CO}(J = 2-1)$ , (b)  $^{13}\text{CO}(J = 2-1)$ , and  $\text{C}^{18}\text{O}(J = 2-1)$  line emission toward M33GMC 37. Each panel shows intensity distribution integrated every  $5 \text{ km s}^{-1}$  in a velocity range from  $-145$  to  $-125 \text{ km s}^{-1}$ . The contour levels are  $4, 8, 14, 22, 32, 44, 58$ , and  $74 \text{ K km s}^{-1}$  for  $^{12}\text{CO}(J = 2-1)$ ;  $2, 4, 8$ , and  $14 \text{ K km s}^{-1}$  for  $^{13}\text{CO}(J = 2-1)$ ; and  $1.5, 2, 3$ , and  $5 \text{ K km s}^{-1}$  for  $\text{C}^{18}\text{O}(J = 2-1)$ . The beam size and scale bar are also shown in the top right corner and bottom left corner, respectively. The crosses indicate the positions of the millimeter continuum sources.

which allows mass growth of stars against the stellar feedback (Inoue & Fukui 2013). For the case of M33GMC 37, the observed velocity separation of red and blue clouds is  $\sim 6 \text{ km s}^{-1}$  (see CO spectra in Figure 2b). Although the velocity separation will be changed due to the projection effect, this is roughly consistent with the typical velocity separation in the Galactic high-mass star forming regions triggered by cloud-cloud collisions: e.g., M20 ( $\sim 7.5 \text{ km s}^{-1}$ , Torii et al. 2011), RCW 36 ( $\sim 5 \text{ km s}^{-1}$ , Sano et al. 2018), M42 ( $\sim 7 \text{ km s}^{-1}$ , Fukui et al. 2018a), and RCW 166 ( $\sim 5 \text{ km s}^{-1}$ , Ohama et al. 2018).

We next focus on the velocity structures of colliding two clouds. Previous numerical simulations and observational results demonstrated that colliding clouds create an intermediate velocity component—bridging feature—connecting two clouds due to the deceleration by colli-

sions, if the projected velocity separation is significantly larger than the linewidth of colliding clouds (see Fukui et al. 2018a and references therein). When the two colliding clouds have roughly the same column density of gas, the two clouds will be merged and appears as a single peak CO profile centered at the mean velocity of the two colliding clouds (e.g., Fukui et al. 2017). In the case of M33GMC 37, the  $V_{\text{LSR}} \sim -135 \text{ km s}^{-1}$  feature in the  $^{13}\text{CO}$  spectrum at the position A is possibly a bridging feature (see Figure 2b), but is not significantly detected because of the small velocity separation of the two colliding clouds. However, CO spectra in the position B—the densest part of the colliding clouds—show the single peak CO profiles centered at  $V_{\text{LSR}} \sim -133.5 \text{ km s}^{-1}$ , roughly corresponding to the mean velocity of the red and blue clouds (see also Figure 2c). It is consistent that the two clouds have

roughly the same column density of  $\sim 4\text{--}5 \times 10^{22} \text{ cm}^{-2}$ , assuming the cloud-cloud collision has occurred.

The V-shaped structure in the position-velocity diagram as shown in Figure 5 provides us with suggestive evidence for head-on cloud-cloud collision. As discussed above, an intensity depression or a hole-like structure might indicate the spot of collision between two clouds for the case of the head-on collision. If we make a position-velocity diagram that includes the collision region, we can find not only the bridging feature but also the V-shaped structure in the position-velocity diagram (e.g., Fukui et al. 2018a, 2018c, 2018d; Hayashi et al. 2018; Torii et al. 2018a, 2018b; Fujita et al. 2019b). Note that if the oblique collision—e.g., collisions with the edges of the clouds—occurred, we could not find such a V-shaped structure in the position-velocity diagram (Fujita et al. 2020). For M33GMC 37, we can clearly see the V-shaped structure connecting the red and blue clouds as the intermediate velocity component that is called the bridging feature. Moreover, the presence of an intensity peak and depression in the V-shaped structure is predicted by the synthetic observations of a theoretical result of the head-on cloud-cloud collision (e.g., Fukui et al. 2018c).

Another important signature of a collision is complementary spatial distribution of colliding clouds. In general, colliding clouds are not the same size, such as simulated by Habe & Ohta (1992) and Anathpindika (2010). In fact, observational results indicate that colliding clouds have different sizes, morphologies, and density distributions (e.g., Hasegawa et al. 1994; Furukawa et al. 2009; Fukui et al. 2014, 2018a, 2018b; Enokiya et al. 2018, Tokuda et al. 2018, Dewangan et al. 2019a, 2019b). In such cases, one of the colliding clouds can create a hole-like structure in the other cloud, if the colliding cloud has a denser part and/or smaller size than the other cloud. This produces the complementary spatial distribution of two clouds with different systematic velocity. Furthermore, the angle of two colliding clouds  $\theta$  is generally not 0 degrees or 90 degrees relative to the line-of-sight. It means that we can also observe a spatial displacement between the complementary distributions of two clouds.

To evaluate such complimentary distributions of colliding two clouds, it is useful to calculate the correlation coefficient between the intensity distributions of two clouds (c.f., S. Fujita et al. in preparation). If the correlation coefficient between the two colliding clouds shows a negative value, the two clouds show complementary spatial distributions. The lower the correlation coefficient, the higher is complementarity. By changing values of spatial displacement for one of the colliding clouds, we can obtain a map of correlation coefficient between the two clouds as a func-

tion of displacement. The best-fit value of the displacement for each coordinate can be derived as the point of the local minimum.

In M33GMC 37, we find complementary spatial distributions of red and blue clouds by following the above method. Figure 8a shows the map of blue cloud superposed on the red cloud contours with the spatial displacement of  $\sim 6.2 \text{ pc}$  toward the direction of southeast. The brightest peak of the red cloud is fits within the hole-like structure of the blue cloud. The second and third minor peaks of the red cloud also show good complementary distributions (or anti-correlation) with the blue cloud. Figure 8b shows the map of correlation coefficient between the two clouds as the function of spatial displacement of the red cloud in the directions of Right Ascension and Declination. Since the cloud-collision in M33GMC 37 is likely the head-on collision, the correlation coefficients were calculated toward inner parts of the blue cloud. We can find the local minimum with the correlation coefficient of  $-0.44$  at a shift by 15 pix in R.A. and  $-12 \text{ pix}$  in Dec., which is significantly lower than the correlation coefficient of  $-0.05$  without displacement. We also calculate P-value which provides information about whether a statistical hypothesis is significant or not. As a result, the correlation coefficient of  $-0.44$  is significant at the 0.5% significance level.

If the cloud-collision scenario is correct, we can also estimate the collision time scale as a dynamical time scale using the values of displacement and velocity difference of two clouds to be  $(\text{spatial displacement}) / (\text{velocity difference}) = 8.8 \text{ pc} / 8.5 \text{ km s}^{-1} \sim 1 \text{ Myr}$  assuming the collision angle  $\theta = 45$  degree. Since GMCs are thought to be dispersed within  $\sim 1.5 \text{ Myr}$  due to strong stellar winds and UV radiation (Kruijssen et al. 2019), the shorter collision time scale is consistent with the presence of dense molecular clouds surrounding the high-mass stars and small H $\alpha$  regions with a few pc extent in H $\alpha$  emission because of young age of the high-mass stars (see Figures 1b and 4).

We also note that the number of high-mass stars ( $\lesssim 10$ ) in M33GMC 37 is consistent with previous observational studies of cloud-cloud collisions. According to Fukui et al. (2018a), the formation of super star clusters containing more than ten O-type stars requires collisions of two dense clouds, one of which has a high column density of at least  $\sim 10^{23} \text{ cm}^{-2}$  (e.g., RCW 38, Fukui et al. 2016; NGC 3603, Fukui et al. 2014; Westerlund 2, Furukawa et al. 2009). On the other hand, the formation of single or a few O-type stars happens in a collision between molecular clouds with low column density of several  $10^{22} \text{ cm}^{-2}$  or less (e.g., RCW 120, Torii et al. 2015; NGC 2359, Sano et al. 2017b; S44, Kohno et al. 2018b; N4, Fujita et al. 2019a, more de-

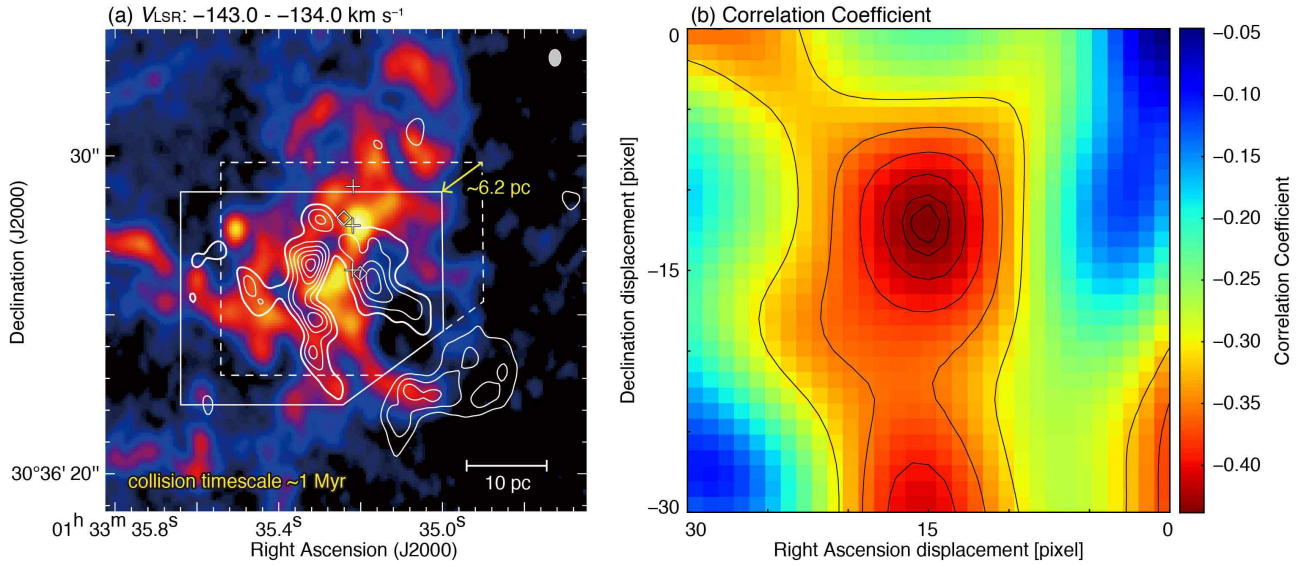


**Fig. 8.** (a) Complementary spatial distribution of red cloud (contours) and blue clouds (image). The velocity ranges of image and contours are the same as shown in Figures 4a and 4b, respectively. The contour levels are 16, 26, 36, 46, 56, and 66  $\text{K km s}^{-1}$ . The contours are spatially displaced  $\sim 6.2$  pc in the direction of southeast (P. A. = 137 degree). The dashed and solid rectangles indicate before and after displacement of the contours, respectively. The crosses and diamonds are the same as shown in Figure 2. The scale bar and beam size are also shown in the bottom and top right corners, respectively. (b) Map of Pearson's correlation coefficient as a function of displacements in Right Ascension direction and in the Declination direction in the unit of pixel. The size of a pixel is 84.5 mas. The origin of coordinates is  $(\alpha_{\text{J2000}}, \delta_{\text{J2000}}) = (01^{\text{h}}33^{\text{m}}35\overset{\text{s}}{.}22, 30^{\circ}36'27\overset{\text{s}}{.}5)$ . The intensity distributions of  $^{12}\text{CO}(J = 2-1)$  enclosed by the dashed polygon (blue cloud) and the solid polygon (red cloud) were used to calculate the correlation coefficient. Superposed contours indicate the values of correlation coefficients, whose levels are from  $-0.435, -0.430, -0.415, -0.390, -0.355$ , and  $-0.310$ .

tailed results are summarized in Enokiya et al. 2019). For M33GMC 37, the two colliding clouds have a low column density of  $\sim 4\text{--}5 \times 10^{22} \text{ cm}^{-2}$ . Therefore, cloud-cloud collisions in M33GMC 37 can create  $\sim 10$  high-mass stars at most. This is consistent with  $\sim 10$  stars that are detected by *HST* optical images within the KPNO H $\alpha$  boundary (see Figure 6).

In addition, Enokiya et al. (2019) recently revealed that the number of OB stars formed in cloud collisions depends not only on the column density, but also on the velocity difference of the two colliding clouds. Figure 9 shows the correlation plot between the column density and relative velocity toward the sites of cloud-cloud collisions in the Milky Way (Enokiya et al. 2019). The authors found that too fast or slow cloud collisions cannot form OB stars even if the cloud column density is high enough. In the case of M33GMC 37, the observational parameters are consistent with the trend seen in previous studies. This possibly indicates that there is no critical difference between the Milky Way and M33 from the view point of high-mass star formation triggered by cloud-cloud collisions. To evaluate the interpretation, more evidence on triggered high-mass star formation via cloud-cloud collisions is needed. Future ALMA observations of young massive clusters in M33 will allow us to study detailed processes of high-mass star formation.

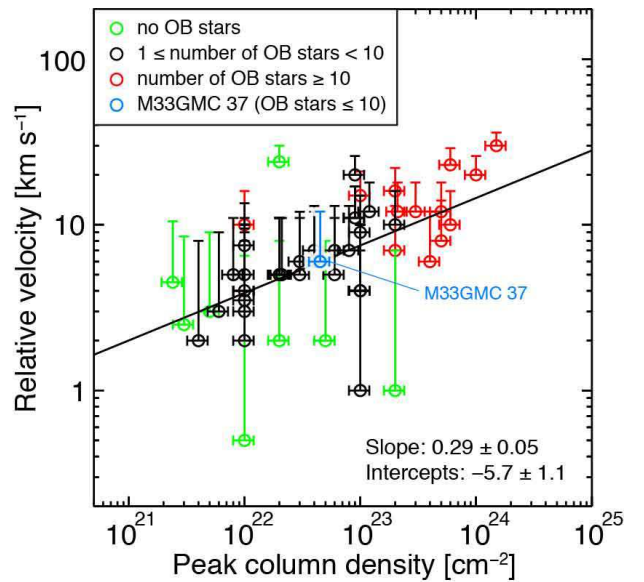


**Fig. 9.** Scatter plot between the peak column density of molecular hydrogen and relative velocity of colliding two clouds toward the sites of cloud-cloud collisions in the Milky Way (Enokiya et al. 2019). The green, black, and red circles represent the H $\alpha$  regions associated with no OB stars, less than ten OB stars, and more than ten OB stars, respectively. The solid line indicates the regression line obtained by least-squares fitting (Enokiya et al. 2019). We also added the data point of M33GMC 37 as the cyan circle.

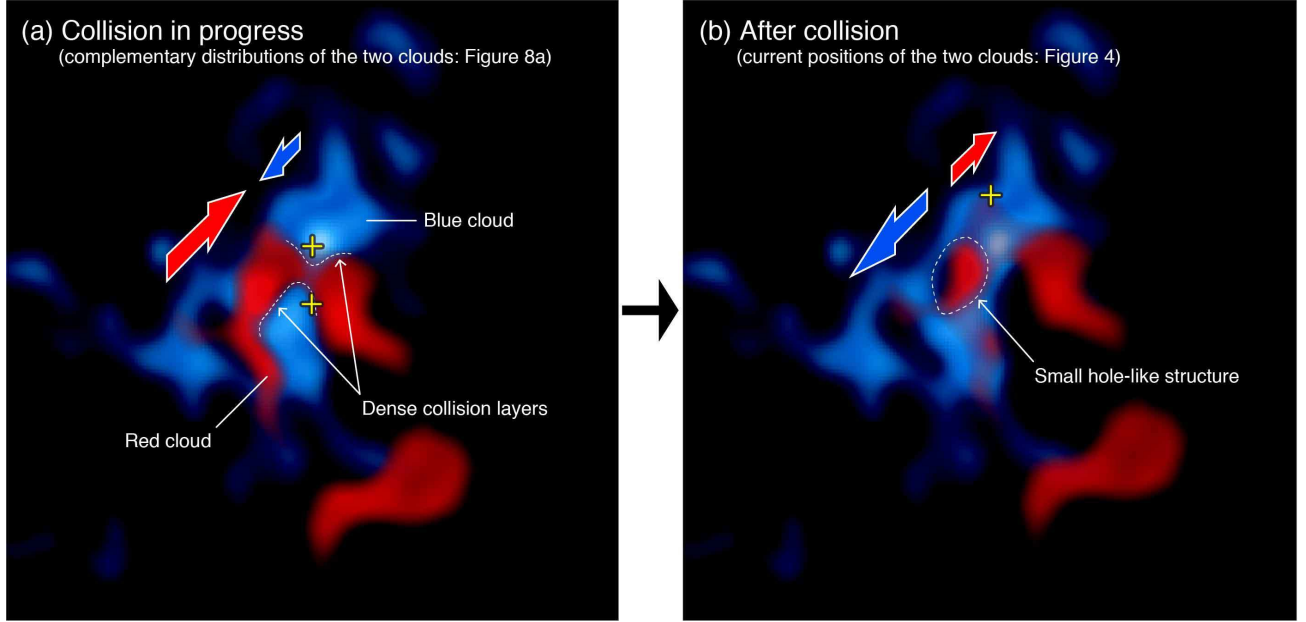


**Fig. 10.** Schematic images of the cloud-cloud collisions in M33GMC 37 for the phases of (a) collision in progress and (b) after collision. The red and blue colors represent the red and blue clouds, respectively. The red and blue arrows indicate the moving directions of the red and blue clouds, respectively. The dense collision layers and the small hole-like structure in the blue cloud are also indicated. The yellow crosses indicate the positions of MMSs 1–3.

Finally, we present a summary picture of the high-mass star formation triggered by the cloud collisions in M33GMC 37. Figure 10 shows schematic images of the cloud-cloud collisions in M33GMC 37. First, the red and blue clouds were moving in the direction approaching each other with a relative velocity of more than  $6 \text{ km s}^{-1}$  respect to the line of sight. Next, the two clouds collided with each other  $\sim 1 \text{ Myr}$  ago. The continuous collisions created the complementary spatial distributions between the two clouds (Figures 10a and 8a). The molecular gas was efficiently compressed especially in the dense collision layers, which formed the high-mass stars toward MMSs 2 and 3 (yellow crosses). Finally, the red cloud penetrated the blue cloud making the small hole-like structure and moved behind the blue cloud, which corresponds to the present positions of the two clouds (Figures 10b and 4). The high-mass star in MMS 1 might have formed recently when the edge of the red cloud finally reached the position of MMS 1. The bright spot and cavity structure in the position–velocity diagram are also consistent with the positions of the dense collision layers and the hole-like structure in the blue cloud, respectively (Figure 5).

To summarize, the red and blue clouds in M33GMC 37 fulfill four requirements of high-mass star formation triggered by cloud-cloud collisions as follows: (1) a super sonic velocity separation of two clouds, (2) complementary spatial distribution with a displacement of colliding clouds, (3) a presence of a bridging feature connecting the two clouds in velocity space, and (4) V-shaped structure

in the position–velocity diagram. We therefore suggest that the high-mass stars corresponding to ten B0V–O7.5V types in M33GMC 37 were formed by cloud-cloud collisions. Further ALMA observations of M33 GMCs will allow us to study high-mass star formation via the cloud-cloud collisions in the spiral galaxy, the results of which can be directly compared with that of the Milky Way and Magellanic Clouds.

## 5 Conclusion

In the present study, we carried out new CO( $J = 2-1$ ) and continuum observations of M33GMC 37 using ALMA with the angular resolution of  $\sim 0''.5$ , corresponding to the spatial resolution of  $\sim 2 \text{ pc}$  at the distance of M33. We revealed two individual molecular clouds with a velocity separation of  $\sim 6 \text{ km s}^{-1}$  that are associated with up to  $\sim 10$  high-mass stars having the spectral types of B0V–O7.5V. The two molecular clouds show complementary spatial distribution with the spatial displacement of  $\sim 6.2 \text{ pc}$ . The intermediate velocity component of the two clouds as the V-shaped structure in the position–velocity diagram is also detected. We propose a possible scenario that the high-mass stars in M33GMC 37 were formed by cloud-cloud collisions approximately 1 Myr ago.

## Acknowledgments

This paper makes use of the following ALMA data: ADS/JAO ALMA#2018.1.00378.S. ALMA is a partnership of ESO (representing its member states), NSF (USA) and NINS (Japan), together with NRC (Canada) and NSC and ASIAA (Taiwan) and KASI (Republic of Korea), in cooperation with the Republic of Chile. The Joint ALMA Observatory is operated by ESO, AUI/NRAO, and NAOJ. Based on observations made with the NASA/ESA Hubble Space Telescope, and obtained from the Hubble Legacy Archive, which is a collaboration between the Space Telescope Science Institute (STScI/NASA), the Space Telescope European Coordinating Facility (ST-ECF/ESA) and the Canadian Astronomy Data Centre (CADC/NRC/CSA). This study was financially supported by Grants-in-Aid for Scientific Research (KAKENHI) of the Japanese Society for the Promotion of Science (JSPS, grant Nos. 16K17664, 18J01417, and 19K14758). K. Tokuda was supported by NAOJ ALMA Scientific Research Grant Number of 2016-03B. H.S. was also supported by the ALMA Japan Research Grant of NAOJ Chile Observatory (grant No. NAOJ-ALMA-226). M.S. acknowledges support by the Deutsche Forschungsgemeinschaft through the Heisenberg professor grants SA 2131/5-1 and 12-1. We are also grateful to the anonymous referee for useful comments which helped the authors to improve the paper.

## References

Anathpindika, S. V. 2010, MNRAS, 405, 1431

Cornwell, T. J. 2008, IEEE Journal of Selected Topics in Signal Processing, 2, 793

Dewangan, L. K., Ojha, D. K., Baug, T., et al. 2019a, ApJ, 875, 138

Dewangan, L. K., Sano, H., Enokiya, R., et al. 2019b, ApJ, 878, 26

Druard, C., Braine, J., Schuster, K. F., et al. 2014, A&A, 567, A118

Enokiya, R., Sano, H., Hayashi, K., et al. 2018, PASJ, 70, S49

Enokiya, R., Torii, K., & Fukui, Y. 2019, PASJ, doi:10.1093/pasj/psz119

Freedman, W. L., Madore, B. F., Gibson, B. K., et al. 2001, ApJ, 553, 47

Fujita, S., Tsutsumi, D., Ohama, A., et al. 2017, arXiv e-prints, arXiv:1706.05664

Fujita, S., Torii, K., Tachihara, K., et al. 2019a, ApJ, 872, 49

Fujita, S., Torii, K., Kuno, N., et al. 2019b, PASJ, 46

Fujita, S., Tsutsumi, D., Ohama, A., et al. 2020, PASJ, doi:10.1093/pasj/psaa005

Fukui, Y., Sano, H., Sato, J., et al. 2012, ApJ, 746, 82

Fukui, Y., Ohama, A., Hanaoka, N., et al. 2014, ApJ, 780, 36

Fukui, Y., Harada, R., Tokuda, K., et al. 2015, ApJL, 807, L4

Fukui, Y., Torii, K., Ohama, A., et al. 2016, ApJ, 820, 26

Fukui, Y., Tsuge, K., Sano, H., et al. 2017, PASJ, 69, L5

Fukui, Y., Torii, K., Hattori, Y., et al. 2018a, ApJ, 859, 166

Fukui, Y., Kohno, M., Yokoyama, K., et al. 2018b, PASJ, 70, S41

Fukui, Y., Kohno, M., Yokoyama, K., et al. 2018c, PASJ, 70, S44

Fukui, Y., Ohama, A., Kohno, M., et al. 2018d, PASJ, 70, S46

Fukui, Y., Tokuda, K., Saigo, K., et al. 2019, ApJ, 886, 14

Furukawa, N., Dawson, J. R., Ohama, A., et al. 2009, ApJL, 696, L115

Gaia Collaboration, Brown, A. G. A., Vallenari, A., et al. 2018, A&A, 616, A1

Gratier, P., Braine, J., Rodriguez-Fernandez, N. J., et al. 2010, A&A, 522, A3

Gratier, P., Braine, J., Rodriguez-Fernandez, N. J., et al. 2012, A&A, 542, A108

Habe, A., & Ohta, K. 1992, PASJ, 44, 203

Hasegawa, T., Sato, F., Whiteoak, J. B., et al. 1994, ApJL, 429, L77

Hayashi, K., Sano, H., Enokiya, R., et al. 2018, PASJ, 70, S48

Inoue, T., & Fukui, Y. 2013, ApJL, 774, L31

Inoue, T., Hennebelle, P., Fukui, Y., et al. 2018, PASJ, 70, S53

Kohno, M., Torii, K., Tachihara, K., et al. 2018a, PASJ, 70, S50

Kohno, M., Tachihara, K., Fujita, S., et al. 2018b, PASJ, 126

Kruyssen, J. M. D., Schruba, A., Chevance, M., et al. 2019, Nature, 569, 519

Kudritzki, R.-P., & Puls, J. 2000, ARA&A, 38, 613

Massey, P., Olsen, K. A. G., Hodge, P. W., et al. 2006, AJ, 131, 2478

Martins, F., Schaefer, D., & Hillier, D. J. 2005, A&A, 436, 1049

Mayya, Y. D., & Prabhu, T. P. 1996, AJ, 111, 1252

McMullin, J. P., Waters, B., Schiebel, D., Young, W., & Golap, K. 2007, Astronomical Data Analysis Software and Systems XVI, 376, 127

Miura, R. E., Kohno, K., Tosaki, T., et al. 2012, ApJ, 761, 37

Ohama, A., Kohno, M., Fujita, S., et al. 2018, PASJ, 70, S47

Saigo, K., Onishi, T., Nayak, O., et al. 2017, ApJ, 835, 108

Sano, H., Reynoso, E. M., Mitsuishi, I., et al. 2017a, Journal of High Energy Astrophysics, 15, 1

Sano, H., Torii, K., Saeki, S., et al. 2017b, arXiv e-prints, arXiv:1708.08149

Sano, H., Enokiya, R., Hayashi, K., et al. 2018, PASJ, 70, S43

Shima, K., Tasker, E. J., Federrath, C., et al. 2018, PASJ, 70, S54

Tachihara, K., Gratier, P., Sano, H., et al. 2018, PASJ, 70, S52

Takahira, K., Tasker, E. J., & Habe, A. 2014, ApJ, 792, 63

Tokuda, K., Onishi, T., Saigo, K., et al. 2018, ApJ, 862, 8

Tokuda, K., Fukui, Y., Harada, R., et al. 2019, ApJ, 886, 15

Torii, K., Enokiya, R., Sano, H., et al. 2011, ApJ, 738, 46

Torii, K., Hasegawa, K., Hattori, Y., et al. 2015, ApJ, 806, 7

Torii, K., Hattori, Y., Matsuo, M., et al. 2018a, PASJ, 121

Torii, K., Fujita, S., Matsuo, M., et al. 2018b, PASJ, 70, S51

Tosaki, T., Kuno, N., Onodera, S. M., et al. 2011, PASJ, 63, 1171

Tsuge, K., Sano, H., Tachihara, K., et al. 2019, ApJ, 871, 44

Verley, S., Hunt, L. K., Corbelli, E., et al. 2007, A&A, 476, 1161

Zinnecker, H., & Yorke, H. W. 2007, ARA&A, 45, 481